Catalysis Science & Technology

ROYAL SOCIETY OF CHEMISTRY

PAPER

View Article Online
View Journal | View Issue

Cite this: *Catal. Sci. Technol.*, 2021, 11, 4898

Coordinately unsaturated O_{2c}–Ti_{5c}–O_{2c} sites promote the reactivity of Pt/TiO_2 catalysts in the solvent-free oxidation of *n*-octanol†

Pengfei Yang,[a] Mark Douthwaite, [b] Jiahao Pan,[a] Lirong Zheng, [c] Song Hong, [a] David J. Morgan, [b] Mingyu Gao,[a] Dianqing Li, [a] Junting Feng *[a] and Graham J. Hutchings *[b]

A series of TiO_2 anatase materials were synthesized with varying proportions of exposed (101) and (001) facets. Pt was subsequently impregnated onto these materials, which were then exposed to either an aerobic or reductive thermal treatment. The final catalysts were assessed for their performance in the aerobic, solvent free oxidation of octanol. Many kinds of characterization methods were employed to gain insight on how the exposed support facets influenced the catalysis. Thermal reduction of the catalysts led to a loss in the support surface structure, but in the contrary, after calcination, the defined facets remained, which was revealed by Raman and XRD. We further provide evidence that the coordinately unsaturated O_{2c}–Ti_{5c}–O_{2c} sites present in the support promoted the dispersion of Pt after calcination in air, leading to the formation of low-coordinated and electron-deficient Pt clusters, based on high resolution- and spherical- aberration corrected transmission electron microscopy and X-ray absorption fine structure analysis. The calcined catalysts were far more active for both the oxidation of octanol and intermediate octanal, thus resulting in a higher selectivity of octanoic acid. Catalyst performance closely correlated with the proportion of low-coordinated Pt species and the specific surface coordination structure of the support in the catalyst. Subsequent *in situ* Fourier transfer infrared experiments, conducted using alcohol and aldehydic probe molecules, confirmed that substrate adsorption was strongly influenced by the low-coordinated sites of both the Pt cluster and the exposed surface facets on the support.

Received 17th April 2021,
Accepted 6th June 2021

DOI: 10.1039/d1cy00686j

rsc.li/catalysis

Introduction

Alcohol oxidation is an important reaction in organic synthesis as it is a key pathway to produce a variety of fine chemicals such as ketones, aldehydes and carboxylic acids. This is most pertinent, as these products have far reaching industrial applications.[1–4] The use of supported metal materials to catalyze these processes under aerobic conditions has attracted much attention, owing to their often-excellent performance in these reactions and the ease in which they can be separated from the post reaction solution.[5]

Many previous studies have investigated the use of supported metal catalysts for liquid phase alcohol oxidations, under both aqueous and solvated conditions.[6] Examples of alcohol oxidation reactions carried out in the absence of solvent however, are scarcer by comparison. This is particularly true for the oxidation of large aliphatic alcohols, such as octanol,[7–10] decanol[11,12] and 1-dodecanol.[11,13] Previously, researchers have employed noble metal supported catalysts for the oxidation of octanol,[7–10] but in the vast majority of cases, only modest activities are observed. Although no clear evidence has been demonstrated eluding to why the oxidation of such substrates is so challenging, it is likely to be attributed to both steric hindrance from the alkyl chain and electronic donation from the alkyl chain to the alcohol moiety, making activation of the alcohol more difficult. The rate of oxidation then, is likely to be significantly influenced by the nature of the catalytic active sites.

Over supported metal heterogeneous catalysts, alcohol oxidation proceeds through several sequential steps. First, the alcohol group is deprotonated on the catalyst surface, forming a metal-alkoxide intermediate. This is followed by β-hydride elimination of a hydrogen atom from the α-carbon in the alkoxy intermediate, leaving a surface metal hydride and the associated surface bound formyl intermediate. The

[a] *State Key Laboratory of Chemical Resource Engineering, Beijing University of Chemical Technology, Beijing, People's Republic of China. E-mail: fengjt@buct.edu.cn*
[b] *Max Planck- Cardiff Centre on the Fundamentals of Heterogeneous Catalysis FUNCAT, Cardiff Catalysis Institute, School of Chemistry, Cardiff University, Main Building, Park Place, Cardiff, CF10 3AT, UK. E-mail: hutch@cardiff.ac.uk*
[c] *Institute of High Energy Physics, Chinese Academy of Sciences, Beijing 100049, Beijing, People's Republic of China*

† Electronic supplementary information (ESI) available. See DOI: 10.1039/d1cy00686j

latter can either desorb or undergo sequential oxidation to the associated carboxylic acid *via* geminal diol dehydration.[14] Oxidation of the metal hydride with O_2, leads to the formation of water, thus, completing the catalytic cycle. The ease in which the preceding steps occur over a specific catalyst, is what ultimately dictates the catalytic performance observed.[7,15] Given that electronic donation from the alkyl chain is likely to inhibit activation in large aliphatic alcohols, it is particularly important to develop catalysts which can effectively promote both the alcohol dissociation and β-hydride elimination.

Previously, it has been demonstrated that the morphology of supported metal particles can have a dramatic influence on their catalytic reactivity.[16–20] Liu *et al.*[21] previously determined that Pd {111} facets were more effective for the oxidation of 5-hydroxymethyl-2-furfural, than Pd {100} facets. Furthermore, the {111} facet was determined to be highly selective for the oxidation of the intermediate product, 5-hydroxymethyl-2-furancarboxylic acid, to 5-formyl-2-furancarboxylic acid. This was attributed to a reduced energy barrier for this process, proposed to stem from the superior ability of O_2 to reduce to peroxide on these sites. In addition to particle morphology, some works have highlighted that exposed facets on the catalyst support can also influence reactivity in catalytic reactions. We recently demonstrated that crystal-plane support effects in Au_1Pt_3/TiO_2 catalysts influenced reaction selectivity in aerobic glycerol oxidation.[22] We determined that exposed (001) facets on the TiO_2 support promoted the adsorption of the aldehyde functionalities, resulting in a higher reaction selectivity to carboxylic acid products.

From a microstructure perspective, facet-dependent performance is derived from differences in the coordination and arrangement of surface atoms.[23] In addition to influencing the adsorption behavior of reactants, the coordination structure of support could have further impact on the catalytic performance by affecting the properties of the supported metals. For example, Liu *et al.*[17] previously demonstrated that a strong electronic interaction existed between Au nanoparticles and Ti_{5c} species on TiO_2 (100) facets, promoting activity for the oxidation of CO. Our group also observed a similar effect when investigating the interaction between CeO_2 (100) facets and Au_1Pt_3 nanoparticles.[25] We determined that there was a greater electron transfer between the coordinately saturated Ce_{6c}–O_{2c} sites on the support and the Pt component, which promoted glycerol oxidation. Despite the progress made in this field, understanding how different support coordination structures influence the geometric structure of the supported metal particles remains unclear.

Given that the oxidation of large aliphatic alcohols is likely to be inhibited by both steric effects and electron donation from the aliphatic alkyl chain, we consider that such reactions are likely to be highly sensitive to catalyst structure. We therefore synthesize a series of Pt/TiO_2 catalysts, the supports of which, possessed different proportions of exposed (101) and (001) facets, to reveal the effects of the coordination structure of supports on the geometric structure of the supported metal particles. Besides, the catalysts were extensively characterized and tested for the aerobic, solvent free oxidation of octanol, our model large aliphatic substrate. The nature of the exposed surface facets were determined to have a profound effect on both the rate of octanol conversion and the reaction selectivity. We also assessed how the atmosphere used for the thermal treatment of the catalyst, prior to employment in the reaction, influenced performance. Exposing these catalysts to a thermal reductive treatment resulted in a significant loss in the supports surface structure, which dramatically influenced the performance of the catalysts towards octanol oxidation. While, undergoing thermal treatment in air, the catalysts well maintained the original coordination structure of the support, which is considered the precondition for affecting the metal geometric structure.

Results and discussion

A series of TiO_2 materials were first synthesized using an established technique.[22,24,26] HF has previously been incorporated in the synthesis of such materials to serve as a capping agent, which can influence the crystallite structure of the resultant materials. It does this by interacting with the TiO_2 (001) facet, which inhibits the further deposition of Ti species vertically. As such, the (001) facets are stabilized and thus, the exposed surface is a square surface of a truncated octahedral bipyramid. XRD patterns shown in Fig. 1A reveal that the synthesized TiO_2 support materials possess a typical anatase crystal structure (JCPDS No. 21-1272). Interestingly however, as the quantity of HF was increased in the preparation, the intensity and full width at half maximum of some of the reflection change. Notably, the (200) reflection became narrower and the (004) reflection became broader. This indicates that the length in the [100] direction increases and the thickness in the [001] direction decreases, as more HF was used. The Scherrer equation was used to quantify

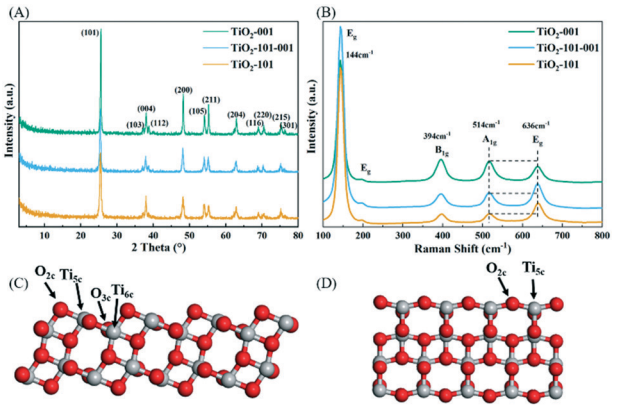

Fig. 1 XRD patterns (A) and Raman spectra (B) for TiO_2 nanocrystals enclosed by different facets. The geometric model and the coordination structure of (C) (101) facet and (D) (001) facet.

Table 1 Information from XRD and physical properties of obtained TiO_2 nanomaterials

Sample	HF (mL)	Average thickness[a] (nm)	Average length[a] (nm)
TiO_2-101	0	29.3 ± 0.5	34.3 ± 3.5
TiO_2-101-001	2	21.5 ± 0.9	46.4 ± 3.4
TiO_2-001	5	23.6 ± 3.7	75.0 ± 10.7

[a] Calculated by Scherrer equation based on the results of XRD.

changes to the crystallite sizes for the three different TiO_2 materials (as shown in Table 1). These measurements show that, in general, as more HF is used in the preparation of these materials, the thickness of the crystallite is reduced from 29.3 to 23.6 nm and the length increases from 34.3 to 75.0 nm. As such, TiO_2 materials with different proportions of exposed (001) facets were successfully prepared.

Illustrative representations of the TiO_2 (101) and (001) surface structures are presented in Fig. 1(C) and (D), respectively. With the TiO_2 (101) facet, there are two types of exposed Ti–O coordination structures, both of which are of equal proportions. One of these has 3 O atoms coordinated to 6 Ti atoms (denoted as O_{3c}–Ti_{6c}) and the other, has 2 O atoms coordinated to 5 Ti atoms (denoted as O_{2c}–Ti_{5c}). In the contrary, with the (001) TiO_2, all of the exposed Ti–O coordination structures exist as O_{2c}–Ti_{5c}.[20] Raman spectroscopy was subsequently employed to further assess the surface structure of these materials. This technique is known to be highly sensitive and can provide information on molecular bonding from a micro-perspective. As shown in Fig. 1B, all the samples exhibit similar peak positions at 144 cm^{-1}, 394 cm^{-1}, 514 cm^{-1} and 636 cm^{-1}, which can be assigned to E_g, B_{1g}, A_{1g} and E_g Raman vibration modes, respectively.[27] It has been reported previously that E_g, B_{1g} and A_{1g} modes are attributed to a symmetric stretching vibration, a symmetric bending vibration, and an asymmetric bending vibration of O–Ti–O, respectively. With more (001) facet exposed, the relative intensity of the B_{1g} (394 cm^{-1}) and A_{1g} modes (514 cm^{-1}) to the E_g mode (636 cm^{-1}), increases. This indicates that there is a higher proportion of symmetric and asymmetric bending on the surface of (001) facet. This, in turn, can be attributed to an increase in unsaturated O_{2c}–Ti_{5c}–O_{2c} sites on the surface of (001) facet, while both saturated O_{3c}–Ti_{6c} and unsaturated O_{2c}–Ti_{5c} sites are present on the surface of (101) facet.

Next, Pt was impregnated onto the different TiO_2 materials and subsequently calcined to produce a series of 1 wt% Pt/TiO_2 catalysts. The actual loading of Pt in the series catalysts were characterized by ICP and listed in Table S1.† All the catalysts has the similar Pt loading which is close to 1%. Furthermore, BET surface area measurements of the TiO_2 support material and the series Pt/TiO_2 are also listed in Table ESI.† The morphology of the supports and supported metal particles were subsequently probed by high resolution transmission electron microscopy (HRTEM) and spherical aberration correction electron microscopy (Cs-TEM). As shown in Fig. 2, the obtained TiO_2 support has an obvious disparity in the arrangement of surface atoms. The lattice fringes of 0.24 and 0.35 nm, with and angle of 68.3°, are observed in Fig. 2A and can be assigned to [001] and [101] directions. This confirms that the surface of the anatase (101) facet is exposed, because of the octahedral structure of anatase. In Fig. 2B, two perpendicular lattice fringes of 0.19 and 0.38 nm, are observed and can be assigned to [100] and [010] (both belong to the <100> family of directions). The orthogonal lattice fringes confirm that this image is representative of a 'top view' of the synthesized TiO_2, whereby, the (001) facet is highly exposed on the top surface of the materials.[28–30] This aligns with the data retrieved from characterization of the TiO_2 supports by Raman spectroscopy and XRD. Although the calcined catalysts, with different facets exposed, possess a similar size of supported nanoparticles (*ca.* 1.7 nm in diameter); determined by HRTEM (Fig. S2†), the results from Cs-TEM also shows that many smaller Pt clusters were also present on the surface of TiO_2 support. As such, it suggests that the Pt particles supported on the (001) facet are smaller than those supported on the (101) facet. This indicates that the Pt atoms may have a stronger interaction with the coordinatively unsaturated sites of the (001) facet.

In addition to calcination, the series of catalyst precursors were also exposed to a thermal reduction. Compared with the

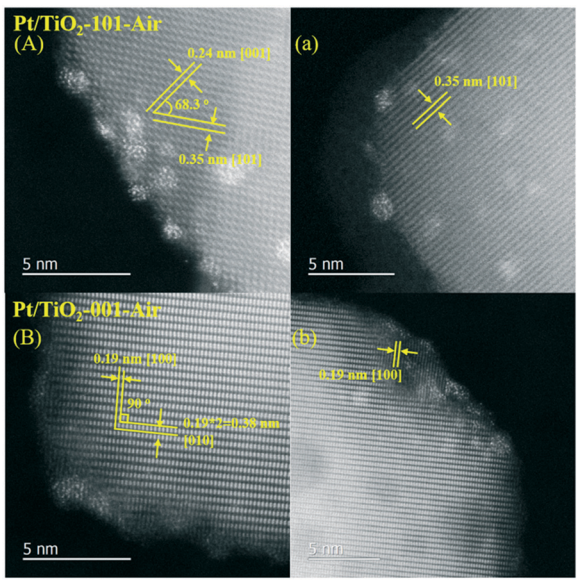

Fig. 2 Cs-TEM images of calcined catalysts of Pt/TiO_2-101-air (A and a) and Pt/TiO_2-001-air (B and b).

Pt cluster formed in calcined catalysts, large Pt nanoparticles are obtain in the reductive atmosphere under the same temperature, as shown in Fig. S3.† Furthermore, the mean size of Pt nanoparticles on (001) facet is 3.24 nm, which is slightly bigger than that on (101) facet (2.50 nm). Previous studies have shown that exposing such precursors to either an aerobic or reductive heat treatment can significantly influence the properties of the resultant catalysts.[31,32] Reductive thermal treatments in particular can lead to SMSI effects, which dramatically influence the morphology at the metal–support interface.[33] To establish how the thermal treatment influenced the electronic structure of these catalysts, each series of catalysts (both after reduction or calcination) was probed by X-ray photoelectron spectroscopy (XPS).

In Fig. 3(A) and (B), a peak is observed at *ca.* 70–80 eV, which is labelled as 'background loss'. This peak is attributed to energy loss structure of the Ti 3s state, and commonly observed in the Pt 4f region when analysing XPS spectra of Pt supported titania catalysts.[34–36] From inspection of the Pt 4f region, it is evident that there are two dominant Pt states are observed, indicative of metallic platinum; observed at *ca.* 70.1 eV and 73.4 eV, assigned to Pt^0 $4f_{7/2}$ and $4f_{5/2}$, and oxidized Pt at *ca.* 71.8 eV and 75.1 eV, assigned to the Pt^{2+} $4f_{572}$ and $4f_{5/2}$ states respectively. As expected, metallic Pt species are dominant in each of the catalysts after thermal reduction in H_2 at 500 °C, whilst Pt^{2+} species are dominant in spectra associated with the calcined catalysts. Besides, the proportion of Pt^{2+} species is also increased from 63% to 82% when the support possesses a higher proportion of exposed anatase (001) facet, as shown in Fig. S4.† It is plausible to suggest that the Pt component has a stronger interaction with (001) facet on which plenty of low-coordinated O atoms are exposed and show more electron-deficient over (001) facet after calcination.

ESI† data, which provided information on the charge and local structure of Pt, was collected by X-ray absorption fine structure (XAFS) at the Pt L_3-edge (11 564 eV) in fluorescence mode. The XANES region can provide information on the oxidation state, through analysis of the white line intensity. In general, the white line intensity in the Pt L_3-edge XANES spectra is dependent on the density of unoccupied states, and often, is used to establish the oxidation state of Pt.[38,45,46] As shown in Fig. 4A, the white line of the calcined Pt/TiO_2 catalyst has a higher intensity relative to the reduced catalysts. Furthermore, the Pt/TiO_2-001-air sample exhibits the highest intensity among the calcined catalysts, indicating that this material possesses the greatest proportion of Pt^{2+}, which aligns with the results from the XPS analysis. EXAFS was further utilized to obtain structural parameters, such as atom coordination numbers and atomic spacing. Analogous k^3-weighed Fourier-transformed EXAFS spectra are shown in Fig. 4B, and the associated fitting parameters are listed in Table 2. The results show that the calcined Pt/TiO_2 catalysts clearly possess Pt–O bonds, with a coordination number of *ca.* 2.7. The intensity at this radial distribution also correlated

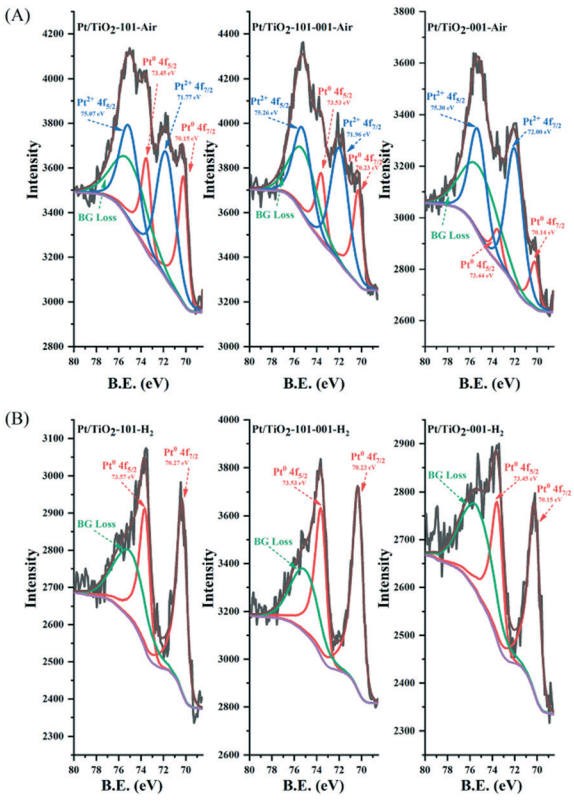

Fig. 3 XPS of spectra series Pt/TiO_2 with different facets exposed (Pt 4f, calcined (A); Pt 4f, reduced (B);).

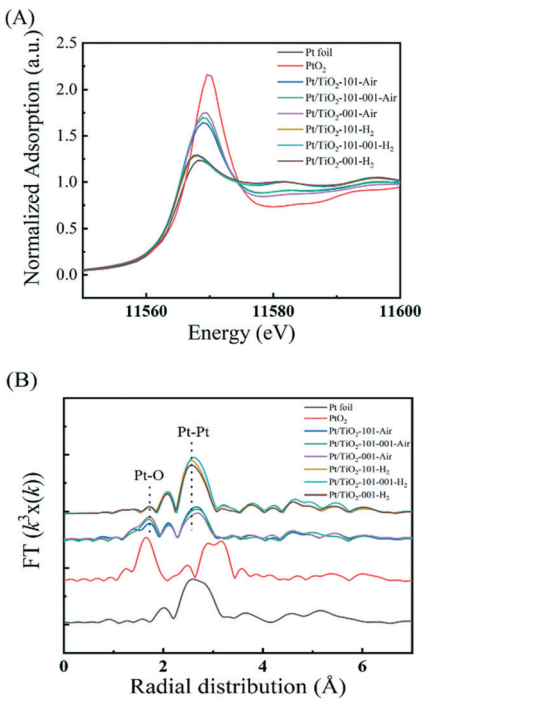

Fig. 4 (A) XANES spectra and (B) the radial distribution functions (RDFs) of the calcined and reduced Pt/TiO_2 with different anatase facets exposed.

Table 2 EXAFS fitting parameters at the Pt L_3-edge for various samples

Sample	Shell	N[a]	R^b (Å)	σ^{2c} (Å^2·10^{-3})	$\Delta E_0{}^d$ (eV)	R factor (%)
Pt/TiO_2-101-air	Pt–O	2.7	1.99	4.3	2.2	1.0
	Pt–Pt	5.2	2.76	4.3	7.6	
Pt/TiO_2-101-001-air	Pt–O	2.6	1.98	1.8	9.6	1.1
	Pt–Pt	4.5	2.77	3.7	0.5	
Pt/TiO_2-001-air	Pt–O	2.8	2.01	2.3	9.4	1.2
	Pt–Pt	3.6	2.76	4.0	8.0	
Pt/TiO_2-101-H_2	Pt–Pt	10.0	2.73	5.3	4.1	0.7
Pt/TiO_2-101-001-H_2	Pt–Pt	10.2	2.75	5.1	6.6	0.5
Pt/TiO_2-001-H_2	Pt–Pt	10.2	2.74	5.8	5.3	0.7

[a] N: coordination numbers; [b] R: bond distance; [c] σ^2: Debye–Waller factors; [d] ΔE_0: the inner potential correction. R factor: goodness of fit. $S02$ were set as 0.84/0.912 for Pt–O/Pt–Pt, which were obtained from the experimental EXAFS fit of reference PtO_2/Pt foil by fixing CN as the known crystallographic value and was fixed to all the samples.

with an increase in the proportion of the (001) facet in the support of the calcined catalysts. A peak which is characteristic of Pt–Pt coordination, centred at *ca.* 2.7 Å, is observed in the radial distribution functions of all the catalysts. However, Pt–Pt bonding is clearly influenced by the atmosphere used for the catalysts thermal treatment and the proportion of (001) facet in the TiO_2 support. As the proportion of the exposed (001) facet increases, the intensity of peak indicative of Pt–Pt bonding reduces. The associated coordination number also decreases from *ca.* 5.2 to 3.6 as the proportion of exposed (001) facet increases in the calcined catalysts. Interestingly however, no difference is observed in the Pt–Pt coordination number in the reduced catalyst, regardless of the proportion of exposed facets in the support material. The differences in Pt–Pt coordination number in the calcined catalyst further underlines that different sized Pt particles are present in these catalysts; a higher proportion of exposed (001) facet evidently promotes Pt dispersion. This in agreement with the results acquired from our Cs-TEM experiments, discussed previously.

From the comprehensive characterization of these catalysts, it's clear that the exposed TiO_2 facets have a dramatic influence on both the geometry and electronic structure of the supported Pt particles. Evidently, increasing the proportion of exposed (001) facets in the support increases the quantity of small, electron deficient Pt clusters after calcination. As such, we propose that the unsaturated O_{2c}–Ti_{5c}–O_{2c} sites, which are the sites situated on the exposed surface of the (001) facets, are responsible for the strong interactions between the support and the Pt component.

To assess what changes to the surface structure occurred, through exposing the catalysts to either aerobic or reductive heat treatments, a series of additional Raman and FTIR spectroscopy experiments were conducted (Fig. 5).

From the Raman spectroscopy experiments (Fig. 5A) it is clear that after Pt loading and calcination, there are no notable changes to the exposed surface facets. On the contrary, after Pt loading and a reductive thermal treatment, all the vibrational peaks exhibit a blue shift. Furthermore, the relative intensity of the E_g (636 cm^{-1}) to A_{1g} (514 cm^{-1}) vibration modes changes; the ratio of E_g to A_{1g} increases after reduction, which is likely indicative of changes in the surface coordination structure, promoted through Pt reduction under a H_2 atmosphere.

Further information on the geometric nature of Pt in the catalysts was acquired from conducting a series of *in situ* CO-FTIR experiments (Fig. 5B). It is important to note that all the reduced Pt/TiO_2 catalysts (Pt/TiO_2–H_2) exhibit a strong IR adsorption due to the formation of Ti^{3+} species during the reductive heat treatment.[40–43] Thus, to amplify the signal observed with these samples, 3 mg of the Pt/TiO_2-001-H_2 catalysts were mixed with 57 mg KBr, pelleted before conducting the experiment. Due to the fact that a comparatively small amount of catalyst was used for these

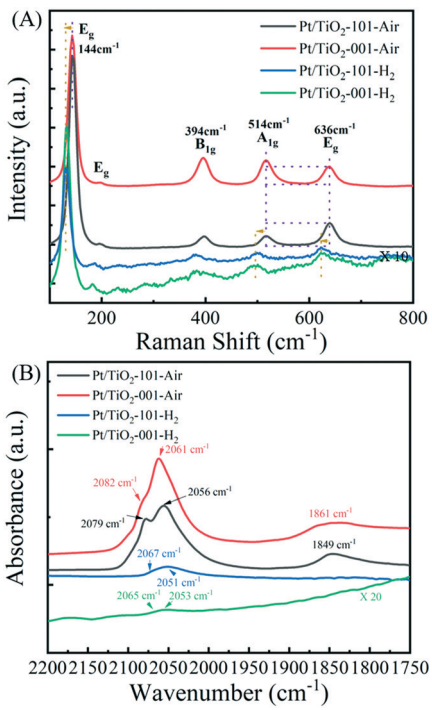

Fig. 5 Raman (A) and *in situ* CO-FTIR spectra (B) of the Pt/TiO_2-101-air, Pt/TiO_2-101-001-air, Pt/TiO_2-101-H_2 and Pt/TiO_2-101-H_2. The signal in the Pt/TiO_2-001-H_2 catalysts DRIFTS spectrum has been amplified 20-fold, for comparative purposes.

experiments, the signal observed for the Pt/TiO_2–H_2 catalysts was significantly lower than that observed over the analogous calcined catalysts. For the calcined catalysts, 60 mg of pure catalyst was pelleted and used in the experiment. However, after amplification of the signal in the corresponding spectrum, similar features are observed to those in the Pt/TiO_2-101-H_2 catalysts spectrum. For the thermally reduced catalysts, Pt/TiO_2-101-H_2 and Pt/TiO_2-001-H_2, the peak observed at *ca.* 2065 cm^{-1} is characteristic of linear CO adsorption on flat Pt surfaces. The peak observed at *ca.* 2082 cm^{-1} is characteristic of linear CO adsorption on low coordinate Pt corner or terrace sites.[37–39,44] No other evidence of CO adsorbed to Pt sites were observed over these catalysts, which suggests that both these materials are comprised of Pt particles with similar geometric structures. Interestingly however, the adsorption bands observed over the analogous calcined catalysts are quite different. Over these catalysts, the bands characteristic of linear CO adsorption on flat and edge sites undergoes a red-shift to 2067 cm^{-1} and 2051 cm^{-1}, indicating that the Pt species in the calcined catalysts are more electron deficient than the analogous Pt species in the reduced catalysts; an observation which is in agreement with our findings from the XPS experiments. It is also evident from these experiments that the calcined Pt/TiO_2-001-air catalyst possesses a higher proportion of linearly adsorbed CO on edge sites to flat sites, than the analogous calcined Pt/TiO_2-101-air catalyst. This suggests that the Pt/TiO_2-101-air catalyst possesses a higher proportion of coordination unsaturated Pt sites, which must be formed on the surface of TiO_2 (001). The lower electron density and higher proportion of co-ordinately unsaturated sites are indicative of a strong interaction between the Pt cluster and anatase (001) facet, suggesting that that coordinative unsaturated site O_{2c}–Ti_{5c}–O_{2c} may have a pivotal role in catalytic performance of this material.

To establish whether this was the case, and to gain further insight on the influence of the atmosphere used for the thermal treatment, the series of materials were employed as catalysts for the oxidation of 1-octanol (Fig. 6). These experiments were all conducted under solvent-free conditions.

Interestingly, all the catalysts exposed to an aerobic thermal heat treatment were notably more active than the analogous catalysts which were thermally reduced (Fig. 6A). Given that the XPS and EXAFS data confirmed that the calcined catalysts comprised of significantly more electron-deficient Pt cluster, its logical to propose that this species is more affective for alcohol oxidation than Pt^0. The rate of octanol conversion was also different over the series of calcined catalysts (solid lines in Fig. 6A), indicating that the exposed support facets influenced reactivity. The rate of reaction was found to correlate with the proportion of exposed (001) in the support. This further confirms that octanol oxidation is promoted by the low-coordinated and

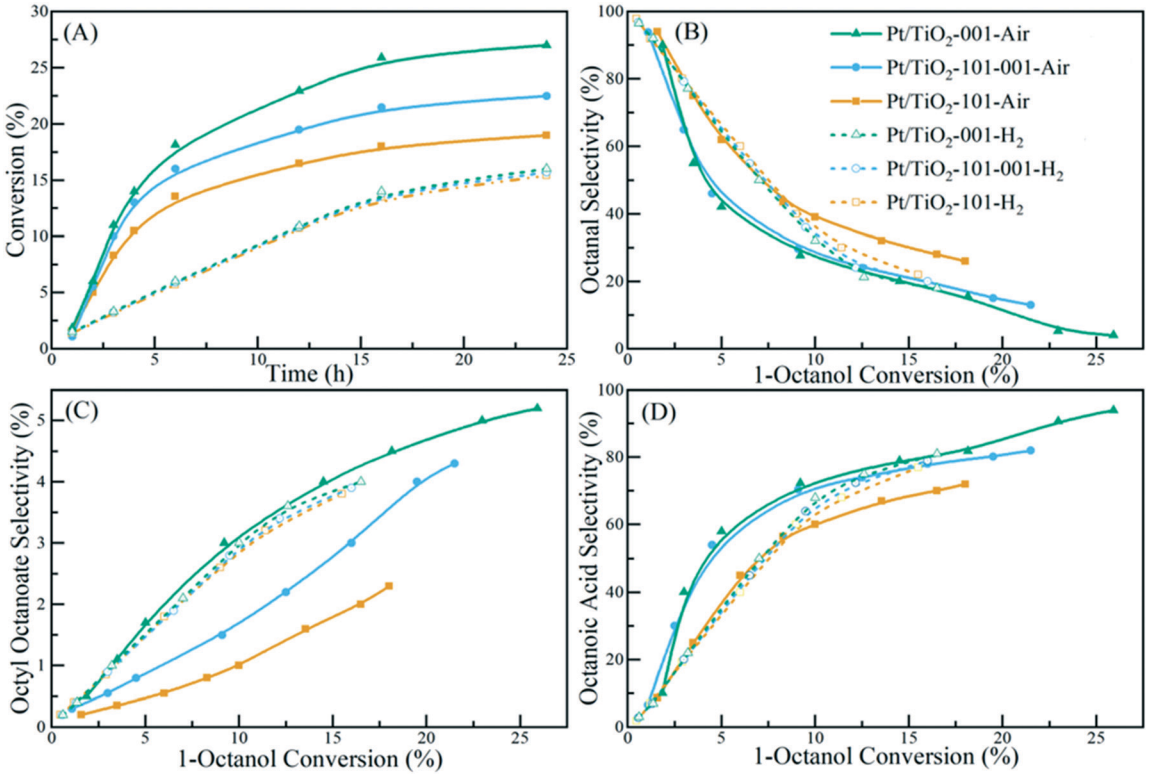

Fig. 6 Curves of 1-octanol oxidation performance over Pt/TiO_2 catalysts with different facets exposed and treated in air and H_2, respectively. The octanol conversion (A) and selectivity to ocatanal (B), octyl octanoate (C) and octanoic acid (D) over each catalyst is displayed. Conditions: 10 mL 1-octanol/metal = 100 000 : 1, 0.1 MPa O_2, T = 100 °C.

electron-deficient Pt cluster species, as we demonstrated that the composition was highest in catalysts whose support possessed a higher proportion of exposed (001) facets.

A similar trend is observed in the associated reaction selectivity data. As with short chain mono-alcohols, 1-octanol first undergoes oxidation to the corresponding aldehyde (octanal), which can be sequentially oxidized through to the corresponding acid (octanoic acid). An additional esterification side reaction can also occur, leading to the formation octyl octanoate. For all the catalysts, at low conversion the primary product is octanal. However, the rate in which this intermediate is oxidized to octanoic acid differs and appears to be dependent on (i) whether the sample was calcined or reduced and (ii) the nature and distribution of the exposed surface facets. Note: only small quantities of octyl octanoate are produced in these reactions; reaction selectivity <6%. As with the oxidation of octanol, the rate of octanal oxidation to octanoic acid is identical for all of the reduced catalysts and a higher rate of conversion is observed over the calcined catalysts (Fig. 6B and C). The rate of octanal oxidation is also highest with the calcined catalyst possessing the greater proportion of the exposed (001) facet.

To gain further insight on the relationship between catalyst structure and catalytic activity, a series of additional *in situ* FTIR experiments were conducted using *n*-propanol as the probe molecule (Fig. 7); propanol was used as the probe molecule for these experiments due to the low vapor pressure of octanol. As with the CO-FTIR experiments (Fig. 5B), a small amount of the Pt/TiO_2-001-H_2 sample was mixed with KBr to amplify the observed signal. This explains why the associated FTIR spectrum (Fig. 6D) is slightly noisier than the other spectra presented (Fig. 7A–C). In Fig. 7(A), the absorption bands observed at 2964 and 2939 cm^{-1} are characteristic of asymmetric stretching of $-CH_3$ and $-CH_2-$ (ν_{as}-CH_3 and ν_{as}-CH_2-) and the adsorption band at 2879 cm^{-1} is attributed to the symmetric stretching of $-CH_3$ (ν_s-CH_3).[45,46] Adsorption bands at 1459, 1402, 1382 and 1364 cm^{-1} are characteristic of asymmetric deformation vibrations of $-CH_3$ (δ_{as}-CH_3), asymmetric deformation vibrations of adsorbed α-CH_2- (δ_{as}-α-CH_2-), symmetric deformation

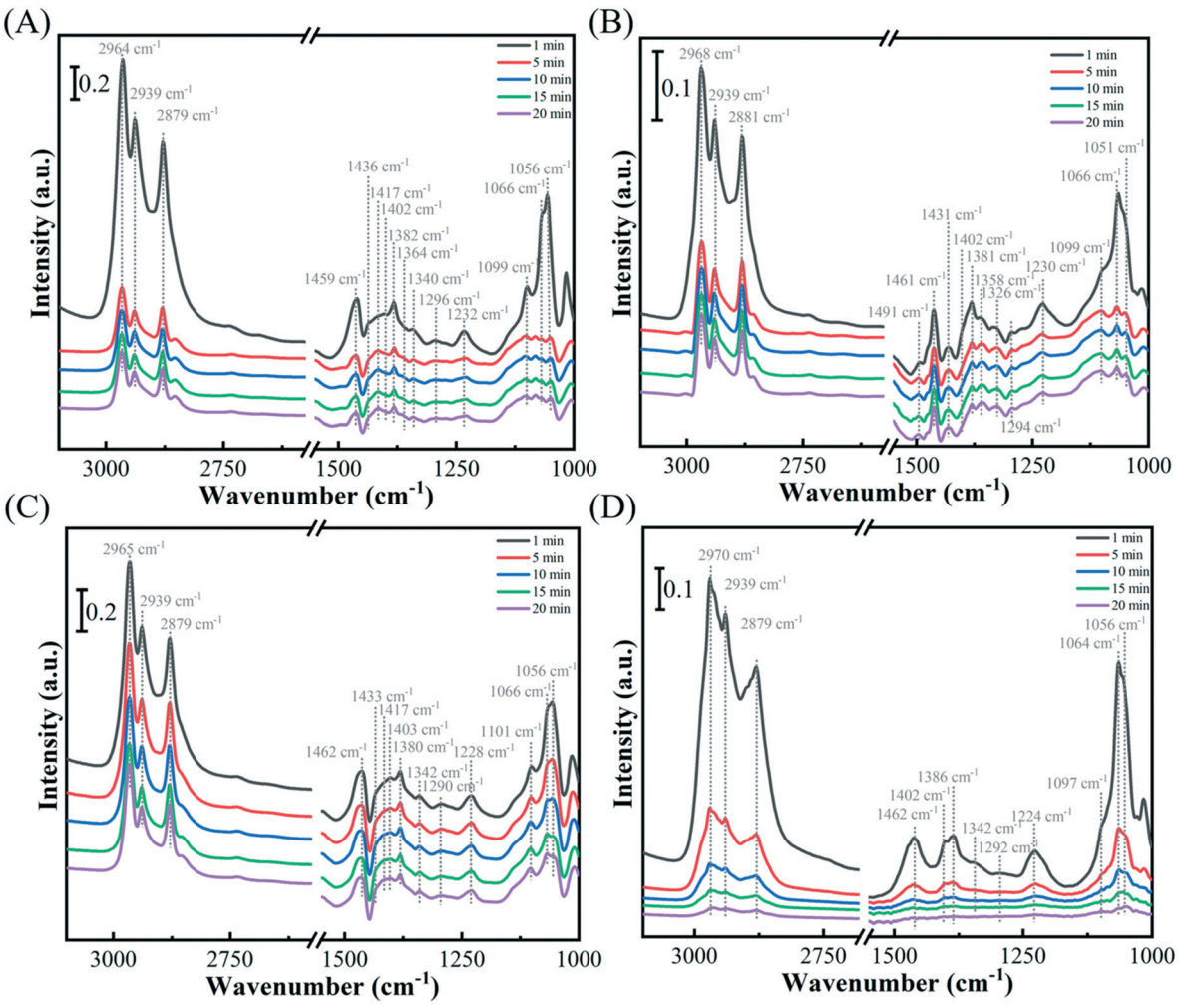

Fig. 7 *In situ* FTIR spectra of propanol adsorption for 30 min followed by desorption at 1, 5, 10, 15 and 20 min on (A) Pt/TiO_2-101-air, (B) Pt/TiO_2-001-air, (C) Pt/TiO_2-101-H_2, (D) Pt/TiO2-001-H_2.

vibrations of $-CH_3$ (δ_s-CH_3), and the symmetric deformation vibrations of adsorbed α-CH_2– (δ_s-α-CH_2–), respectively. The bands at 1340 and 1228 cm^{-1} can be assigned to the δ modes of O–H and C–O stretching (νC–O). The adsorption band at 1100 cm^{-1} can be assigned to the rocking vibration of $-CH_3$ and deformation vibration mode of –C–C–C–O (ω-CH_3 and δ-C–C–C–O), while the adsorption band at 1066 and 1056 cm^{-1} can be assigned to the stretching vibrations of C–C (ν-C–C). Over the calcined Pt/TiO_2-001-air catalyst however, the adsorption band indicative of δO–H incurs a red-shift, from 1340 over Pt/TiO_2-101-air to 1326 cm^{-1}. This indicates that there is an increase in the length of the O–H bond over this material, which could be indicative of a decrease in the bonds associated dissociation energy. Notably, the δ_s-α-CH_2– band also exhibits a slight red shift from 1364 cm^{-1} over Pt/TiO_2-101-air catalyst to 1358 cm^{-1} over Pt/TiO_2-001-air catalyst, indicating that there may be a change in the length of the α-C–H bond. The relative intensity of the δ_s-α-CH_2- band to δ_s-CH_3 over Pt/TiO_2-001-air catalyst is also higher than that of the other catalysts, suggesting there is a greater adsorption of α-C–H bond over the Pt/TiO_2-001-air catalyst. According to the literature,[14] the enhanced adsorption and the dissociation of the α-C–H bond could contribute to the subsequent elimination during the oxidation process and hence the Pt/TiO_2-001-air catalysts achieved a higher conversion of octanol. Furthermore, the formation of metal-alkoxides through hydroxyl group deprotonation, and the subsequent β-hydride elimination, usually occur on the surface of noble metal active sites. Given that the Pt/TiO_2-001-air catalyst possesses a greater proportion of low coordinate Pt clusters, we propose that the higher activity of this catalyst is attributed to the greater proportion of low-coordinated Pt sites it possesses.

Analogous *in situ* FTIR experiments were also conducted using propionaldehyde as the probe molecule (Fig. 8). Again, the Pt/TiO_2-001-H_2 catalyst was mixed with KBr to amplify the signal, which is why much of the features observed in the associated spectrum (Fig. 8D) are indicative of physically adsorbed propionaldehyde. However, some bands indicative of chemisorbed species are visible, allowing for qualitative comparisons to be made with the other catalysts (Fig. 8A–C). Many similar adsorption bands were observed over all the

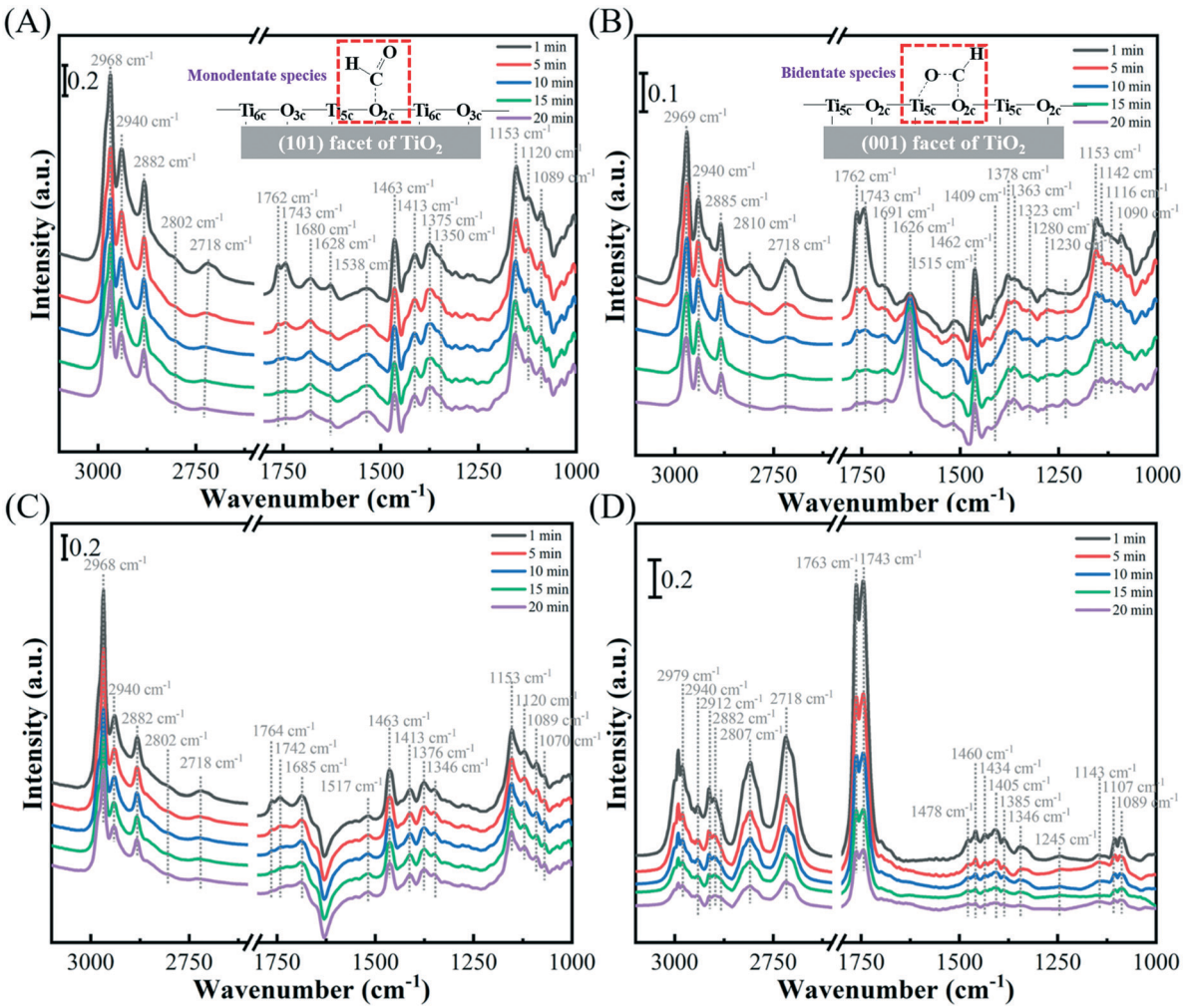

Fig. 8 *In situ* FTIR spectra of propionaldehyde adsorption for 30 min followed by desorption at 1, 5, 10, 15 and 20 min on (A) Pt/TiO_2-101-air, (B) Pt/TiO_2-001-air, (C) Pt/TiO_2-101-H_2, (D) Pt/TiO_2-001-H_2.

catalysts. Adsorption bands indicative of C–H stretching are observed at 2968, 2940 and 2882 cm^{-1}. The bands at *ca.* 1762 and 1743 cm^{-1} can be assigned to the C═O bond of propionaldehyde. However, notable differences are observed in the spectra of the calcined Pt/TiO_2-101-air and Pt/TiO_2-001-air catalysts between 1700 and 1300 cm^{-1}. According to the literature[47–52] and our previous study,[22] the aldehyde group can be adsorbed and dissociated *via* monodentate or bidentate intermediates on the surface of TiO_2 rather than Pt nanoparticles. As shown in Fig. 8A, the adsorption bands at *ca.* 1680 and 1413 cm^{-1} are characteristic of an aldehydic monodentate species over (101) facet of TiO_2. For Pt/TiO_2-001-air catalyst (Fig. 8B), the aldehydic bidentate species are predominant on the surface of (001) some with the adsorption bands at *ca.* 1691 and 1363 cm^{-1}, while only a few of monodentate species exists with a small shoulder peak at 1409 cm^{-1}. Considering the coordination unsaturated O_{2c}–Ti_{5c}–O_{2c} sites of (001) facet, the bidentate species of aldehyde C═O bond of which the C and O atoms is bonded with O_{2c} and the adjacent Ti_{5c} are formed and highly dissociated on (001) facet. For the monodentate species of adsorbed aldehyde group, only the C atom is bonded with O_{2c} site on (101) facet without the participation of the adjacent Ti due to the different coordination structure with (001). Besides, the adsorption bands at *ca.* 1463 and 1375 assigned to the asymmetric and symmetric deformation vibrations of $-CH_3$ (δ_{as}-CH_3 and δ_s-CH_3) are similar over the series catalysts. But the symmetric deformation vibrations of adsorbed α-C–H (δ_s-α-C-H) bond has a red-shift from 1350 cm^{-1} over Pt/TiO_2-101-air to 1323 cm^{-1} over Pt/TiO_2-001-air, indicating a longer length of C–H bond over Pt/TiO_2-001-air catalysts. Similar with the result of propanol FTIR, the prolonged C–H bond would be attributed to its further elimination and hence favours its oxidation to the carboxylic acid products. Furthermore, the intensity of carboxylate species centred at *ca.* 1626 cm^{-1} is increased only Pt/TiO_2-001-air catalyst, which further indicating that (001) facet facilitates the further oxidation of aldehyde group. According to our previous study,[22] although the bidentate species of aldehyde group are adsorbed on the coordination structure of TiO_2 support, the oxidation only happens with the participation of metal active sites. Hence, the low-coordinated Pt active sites could be the reason for the prolonged α-C–H bond of aldehyde, as well as the alcohol.

From the results acquired from these *in situ* FTIR experiments, we propose that low-coordinated Pt clusters promote both the deprotonation of OH group in octanol and the subsequent activation of α-C–H bonds in both octanol and octanal. The O_{2c}–Ti_{5c}–O_{2c} sites in the TiO_2 (001) facet also promote the adsorption and dissociation of the C═O bond, which processed *via* a bidentate intermediate. We propose that this is why a higher reaction selectivity to octanoic acid is observed over this catalyst, when compared at iso-conversion.

The *in situ* FTIR experiments suggest that the activation of both alcohols and aldehydes are promoted by the presence of the exposed (001) facet. Additional kinetic experiments were subsequently conducted to calculate activation energies for both 1-octanol and octanal oxidation over the different calcined catalysts (Fig. S5 and S6†). For both oxidation reactions, the catalyst possessing the support with the most exposed (001) facets exhibited the lowest activation energies, 30.2 and 27.6 KJ mol^{-1} for octanol and octanal oxidation, respectively. The least active catalyst, the support of which possessed the greatest proportion of (101) facets, exhibited activation energies of 39.9 and 40.8 KJ mol^{-1} for octanol and octanal oxidation, respectively. Given that there is a greater difference between the apparent activation energies for the oxidation of octanol, it suggests that the exposed surface facets have a greater influence on formyl oxidation, compared to alcohol oxidation.

On the basis of the above results and the previous studies, a possible mechanism is proposed in Scheme 1. At first, the hydroxyl group of 1-octanol is adsorbed and activated on the surface of low-coordinated and electron-deficient Pt cluster supported on the (001) facet, which promotes the deprotonation of the O–H band and forming an active hydroxyl species with the dissociated O species. The α-C–H of octanol is activated by the low-coordinated Pt cluster following with the β-hydride elimination with the effect of OH* species to form the intermediate product octanal. Then, the aldehyde group of octanal adsorbed on the coordination unsaturated O_{2c}–Ti_{5c}–O_{2c} site of (001) to form a bidentate species while the α-C–H bond of adsorbed aldehyde bidentate species is activated by the nearby low-coordinated Pt cluster. The α-carbon atom of aldehyde group of bidentate species are more active than of monodentate species and benefits the attack of the active hydroxyl species, producing the octanoic acid after the C-H cleavage. Herein, it is an obvious synergetic effect of coordination structure O_{2c}–Ti_{5c}–O_{2c} of (001) facet on support and low-coordinated Pt cluster that facilitate the oxidation of 1-octanol to the final octanoic acid products.

Experimental section

Chemicals

All the materials were analytically pure and employed as received without further purification in our work. Titanium isopropoxide (J&K, 98%, AR), 48 wt% HF(Beijing Tongguang Company), ethanol (Beijing Tongguang Company, 99%, AR) and $H_2PtCl_6{\cdot}6H_2O$ (Tianjin Guangfu Fine Chemical Research Institute, 99.9%, AR) are used.

Preparation of anatase with different facet exposed

The anatase TiO_2 materials, possessing different exposed facets, were prepared by the hydrolysis of titanium isopropoxide with different volumes of HF. The procedure used for the synthesis of TiO_2-101, a TiO_2 anatase material possessing a large proportion of exposed (101) facets, is as follows: titanium isopropoxide (20 mL) and H_2O (2 mL) are mixed and stirred for 30 min under ambient temperature,

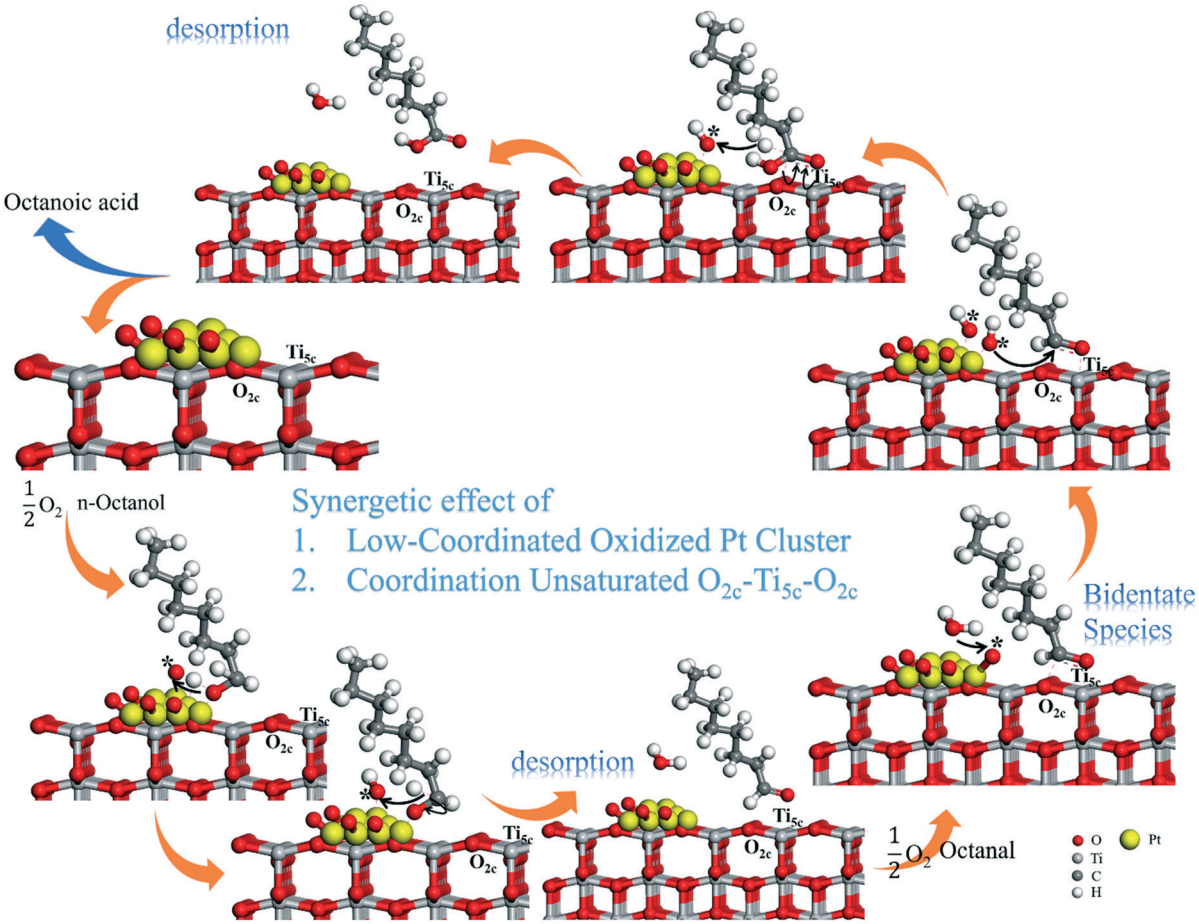

Scheme 1 Possible reaction pathway for the oxidation of 1-octanol over the Pt/TiO_2-001-air catalyst.

after which, the slurry was transfer to a Teflon-lined autoclave and kept at 200 °C for 24 h. After cooling to room temperature, the white precipitate was centrifuged and washed with ethanol (50 mL) for 3 times and DI water until the pH reached 7, before being collected and dried in oven overnight at 80 °C. The final powder was subsequently calcined at 450 °C for 2 h (rate rate = 10 °C min^{-1}). The other anatase TiO_2 materials used in this study, which possess different proportions of exposed {001} facet, were prepared using the same morphology; only different quantities of HF were used. HF (48 wt%) volumes of 2 and 5 mL were used for the synthesis of TiO_2-101-001 and TiO_2-001, respectively.

Preparation of Pt catalysts

An impregnation method was used to prepare the Pt/TiO_2 catalyst precursors. Typically, a known quantity of TiO_2 anatase was dispersed in DI water (10 mL). Aqueous H_2PtCl_6 (30 mM L^{-1}) was then added to this mixture, the volume of which would be sufficient to achieve a final Pt weight loading of 1%. The mixture was then heated to 70 °C under vigorous stirring, until all the water was evaporated. The obtained yellow powder was then separated into two parts; one part was calcined in a tube furnace in air at 500 °C for 5 h (rate rate = 2 °C min^{-1}) and the other, was reduced in a tube furnace under a continuous flow of 10% H_2/Ar (50 mL min^{-1}) at 500 °C for 5 h (rate rate = 2 °C min^{-1}). The catalysts under different treatment condition with different facet exposed are named as Pt/TiO_2-101-air, Pt/TiO_2-101-001-air, Pt/TiO_2-001-air, Pt/TiO_2-101-H_2, Pt/TiO_2-101-001-H_2, and Pt/TiO_2-001-H_2, respectively.

Characterization methods

The crystal structure of the TiO_2 supports and corresponding supported catalysts were assessed by powder X–ray diffraction (XRD) (Shimadzu XRD-600), using a Cu Kα radiation source (λ = 0.154 nm) with a scanning range of 3° to 80° (scan step = 10° min^{-1}). Additional details on the crystal structure of these materials was probed by Raman spectroscopy, using a Renishaw in *Via*-Reflex, instrument with a 633 nm line at room temperature. The morphology of the synthesized TiO_2 and supported Pt species was probed using a JEOL JEM-2100F high-resolution transmission electron microscope (HRTEM). Cs-corrected STEM images were obtained using a JEOL ARM200F microscope equipped with a probe-forming spherical-aberration corrector. The Pt content was measured by a Shimadzu ICPS-7500 inductively coupled plasma

emission spectrometer (ICP-AES). Brunauer–Emmett–Teller (BET) method was employed to calculate the surface area of the samples using a Micromertics Gemini VII2990 instrument with N_2 as the adsorbate at 77 K. X-ray photoelectron spectroscopy (XPS) spectra were collected using a Kratos Axis Supra, using monochromatic Al Kα radiation operating at a power of 150 W (10 mA × 15 kV). High resolution spectra were recorded at a pass energy of 40 eV with a 0.1 eV step size, whilst survey spectra were recorded with a 160 eV pass energy and a 1 eV step size, in both instances the spectrometer was operated in the Hybrid mode, using the Slot aperture defining an analysis area of *ca.* 700 × 300 micron.[2] Charge neutralization was performed using magnetically confined low energy electrons, with charge neutralizer settings of 0.4 A current, a filament bias of 1.0 V and a charge balance of 4.0 V. Quantification was performed using CasaXPS v2.3.24 rev 1.0 W using modified Wagner sensitivity factors as supplied by the instrument manufacturer and after subtraction of a Shirley background. Data was calibrated to the lowest binding energy peak from the fitted C(1s) signal of adventitious carbon and taken to be 284.8 eV, resulting in a Ti($2p_{3/2}$) energy of 458.5 eV as expected for TiO_2. Spectra were fitted using models derived from Pt metal and both Pt and Ti oxide standards using Voigt-type line shapes. Fourier transform infrared spectra (*in situ* FTIR) were recorded using a Bruker Tensor 27 spectrometer fixed with a highly sensitive MCT detector and a heating chamber equipped with KBr windows. In a typical experiment, the samples (60 mg), except for Pt/TiO_2-001-H_2, were first tableted with the IR mold to be used in the later measurements. Due to the poor signal observed with the pure Pt/TiO_2-001-H_2 sample, 3 mg catalyst was mixed with 57 mg KBr before being tableted for the experiment to improve the signal strength. For CO *in situ* FT-IR measurements, the sample was pretreated at 120 °C under a flow of He (40 mL min^{-1}) for 1 h, to remove any gaseous impurities adsorbed on the surface. After collecting the background spectra, the flow was switched to CO, which was passed over the catalyst at a rate of 40 mL min^{-1} for an additional 1 h. The spectra were continuously collected during the absorption of CO until the intensity of absorbed CO stabilised. After removing the gaseous and physisorbed CO, by passing He (40 mL min^{-1}) over the sample for a further 0.5 h, spectra were collected in the range 2000–1000 cm^{-1} with 64 accumulation scans at room temperature. For *in situ* propanol and propyl aldehyde FT-IR experiments, the pretreatment procedures used were the same as that used in the *in situ* CO FTIR experiments. After cooling to room temperature, the background spectra data were collected with a temperature ramp to 100 °C at a rate of 10 °C min^{-1}. After cooling to room temperature again, a flow of He (40 mL min^{-1}) was passed through a bubbler containing either propanol or propionaldehyde before being passed over the sample. Then, spectra were collected in the range of 4000–400 cm^{-1} with accumulation scans every 10 °C as the cell temperature was ramped at a rate of 10 °C min^{-1}.

1-Octanol oxidation

Octanol oxidation reactions were performed in a 50 mL quartz glass reactor equipped with a heating block and magnetic stirrer. First, octanol (10 mL) and a requisite amount of catalyst (octanol/active metal molar ratio was 100 000 : 1) were added to the reactor. The reactor was subsequently purged with a continuous O_2 flow for 30s and finally charged with 1 bar of O_2. The reactor was put into an oil bath on a preheated hot plate (100 °C) and the reaction was left to stir for a specified time (1–24 h). After the reaction was complete, the mixture was rapidly cooled in a cold-water bath and filtered to remove the solid catalyst. Reaction liquid (500 μL) and mesitylene (500 μL) were subsequently mixed and placed into a GC vial. The samples are analyzed by Gas Chromatography (Agilent J&W 7890B) equipped with DB-Wax column (30 × 0.320 mm, df = 0.250 μm) and FID detector. The response factors for each component were determined with standard samples and were used to calculate the conversion and selectivity. In all cases, the carbon balances were 100 ± 5%.

Conclusions

This research clearly illustrates how exposed support facets can influence both metal dispersion and substrate activation. We have demonstrated that the presence of coordinately unsaturated O_{2c}–Ti_{5c}–O_{2c} sites in Pt/TiO_2 catalysts can enhance catalyst performance and influence selectivity in the aerobic oxidation of octanol. Through extensive characterization, we established that these unsaturated sites increased the proportion of low-coordinate, electron deficient Pt species in the catalyst. *In situ* FTIR experiments suggested that low-coordinated Pt clusters promote the activation of the alcohol by assisting with O–H dissociation and β-hydride elimination of hydrogen from the alkoxy intermediate. These experiments also provided insight on why selectivity to octanoic acid was higher over catalysts possessing a larger proportion of O_{2c}–Ti_{5c}–O_{2c} support sites; the sites promote the adsorption and activation of formyl species. The atmosphere used for the catalyst thermal treatment also significantly affected their performance. Exposing the catalysts to a reductive heat treatment, led to a dramatic loss in the support surface structure. Given that the nature of the exposed support sites had such an impact on the catalysis, it was therefore unsurprising that the employment of such heat treatments led to a reduction in catalyst performance. Ultimately, this work highlights how influential the exposed facets of supports are in directing catalysis in liquid phase alcohol oxidation and should be considered for future catalyst design.

Author contributions

P. Y. performed the conceptualization, experimental investigation, the data analysis and the writing of original draft with the help of M. D. M. D. also performed the review

& editing. J. P. performed the oxidation experiments over the series catalysts. L. Z. performed the measurement of XAFS and the results analysis. S. H. performed the measurement of Cs-TEM. D. J. M. performed the analysis of XPS. M. G. performed the measurement of XRD. D. L., J. F. and G. J. H. performed supervision, resources and project administration of this study.

Conflicts of interest

There are no conflicts to declare.

Acknowledgements

This work was supported by the National Natural Science Foundation (22022801, 21878016), National Key Research and Development Program of China (2017YFA0206804), the Fundamental Research Funds for the Central Universities and Cardiff Catalysis Institute. The Pt L_3-edge X-ray adsorption spectra (XAS) were performed at 1W2B beamline at Beijing Synchrotron Radiation Facility (BSRF). XPS data collection was performed at the EPSRC National Facility for XPS ('HarwellXPS'), operated by Cardiff University and UCL, under contract No. PR16195.

Notes and references

1 C. P. Vinod, K. Wilson and A. F. Lee, *J. Chem. Technol. Biotechnol.*, 2011, **86**, 161–171.
2 N. Dimitratos, J. A. Lopez-Sanchez and G. J. Hutchings, *Chem. Sci.*, 2012, **3**, 20–44.
3 H. Song, Z. Liu, Y. Wang, N. Zhang, X. Qu, K. Guo, M. Xiao and H. Gai, *Green Energy Environ.*, 2019, **4**, 278–286.
4 Q. Shang, N. Tang, H. Qi, S. Chen, G. Xu, C. Wu, X. Pan, X. Wang and Y. Cong, *Chin. J. Catal.*, 2020, **41**, 1812–1817.
5 S. E. Davis, M. S. Ide and R. J. Davis, *Green Chem.*, 2013, **15**, 17–45.
6 B. Katryniok, H. Kimura, E. Skrzyńska, J.-S. Girardon, P. Fongarland, M. Capron, R. Ducoulombier, N. Mimura, S. Paul and F. Dumeignil, *Green Chem.*, 2011, **13**, 1960.
7 L. Prati, A. Villa, C. Campione and P. Spontoni, *Top. Catal.*, 2007, **44**, 319–324.
8 T. Ishida, Y. Ogihara, H. Ohashi, T. Akita, T. Honma, H. Oji and M. Haruta, *ChemSusChem*, 2012, **5**, 2243–2248.
9 D. I. Enache, D. W. Knight and G. J. Hutchings, *Catal. Lett.*, 2005, **103**, 43–52.
10 Y. He, J. Feng, G. L. Brett, Y. Liu, P. J. Miedziak, J. K. Edwards, D. W. Knight, D. Li and G. J. Hutchings, *ChemSusChem*, 2015, **8**, 3314–3322.
11 A. Villa, C. E-chan-thaw, M. Schiavoni, S. Campisi, D. Wang and L. Prati, *Cuihua Xuebao/Chin. J. Catal.*, 2014, **35**, 945–951.
12 S. Mori, M. Takubo, K. Makida, T. Yanase, S. Aoyagi, T. Maegawa, Y. Monguchi and H. Sajiki, *Chem. Commun.*, 2009, 5159–5161.
13 V. C. Corberán, M. E. González-Pérez, S. Martínez-González and A. Gómez-Avilés, *Appl. Catal., A*, 2014, **474**, 211–223.
14 S. E. Davis, M. S. Ide and R. J. Davis, *Green Chem.*, 2013, **15**, 17–45.
15 Q. Wang, L. Chen, S. Guan, X. Zhang, B. Wang, X. Cao, Z. Yu, Y. He, D. G. Evans, J. Feng and D. Li, *ACS Catal.*, 2018, **8**, 3104–3115.
16 W. W. Wang, W. Z. Yu, P. P. Du, H. Xu, Z. Jin, R. Si, C. Ma, S. Shi, C. J. Jia and C. H. Yan, *ACS Catal.*, 2017, **7**, 1313–1329.
17 L. Liu, X. Gu, Y. Cao, X. Yao, L. Zhang, C. Tang, F. Gao and L. Dong, *ACS Catal.*, 2013, **3**, 2768–2775.
18 H. Zhang, W. Wang, H. Zhao, L. Zhao, L. Y. Gan and L. H. Guo, *ACS Catal.*, 2018, **8**, 9399–9407.
19 F. Jiang, S. Wang, B. Liu, J. Liu, L. Wang, Y. Xiao, Y. Xu and X. Liu, *ACS Catal.*, 2020, **10**, 11493–11509.
20 A. Chalgin, W. Chen, Q. Xiang, Y. Wu, F. Li, F. Shi, C. Song, P. Tao, W. Shang, J. Wu, J. Wu and J. Wu, *ACS Appl. Mater. Interfaces*, 2020, **12**, 27037–27044.
21 D. Lei, K. Yu, M. R. Li, Y. Wang, Q. Wang, T. Liu, P. Liu, L. L. Lou, G. Wang and S. Liu, *ACS Catal.*, 2017, **7**, 421–432.
22 P. Yang, J. Pan, Y. Liu, X. Zhang, J. Feng, S. Hong and D. Li, *ACS Catal.*, 2019, **9**, 188–199.
23 J. Pan, G. Liu, G. Q. Lu and H. M. Cheng, *Angew. Chem., Int. Ed.*, 2011, **50**, 2133–2137.
24 Y. Zhou, D. E. Doronkin, M. Chen, S. Wei and J. D. Grunwaldt, *ACS Catal.*, 2016, **6**, 7709–7809.
25 X. Zhang, P. Yang, Y. Liu, J. Pan, D. Li, B. Wang and J. Feng, *J. Catal.*, 2020, **385**, 146–159.
26 W. J. Ong, L. L. Tan, S. P. Chai, S. T. Yong and A. R. Mohamed, *Nanoscale*, 2014, **6**, 1946–2008.
27 F. Tian, Y. Zhang, J. Zhang and C. Pan, *J. Phys. Chem. C*, 2012, **116**, 7515–7519.
28 Q. Zhang, J. Luan, X. Huang, Q. Wang, D. Sun, Y. Tang, X. Ji and H. Wang, *Nat. Commun.*, 2020, **11**, 3961.
29 Y. K. Peng, Y. Hu, H. L. Chou, Y. Fu, I. F. Teixeira, L. Zhang, H. He and S. C. E. Tsang, *Nat. Commun.*, 2017, **8**, 675.
30 Y. Xia, K. Zhu, T. C. Kaspar, Y. Du, B. Birmingham, K. T. Park and Z. Zhang, *J. Phys. Chem. Lett.*, 2013, **4**, 2958–2963.
31 M. Fronzi, A. Soon, B. Delley, E. Traversa and C. Stampfl, *J. Chem. Phys.*, 2009, **131**, 104701.
32 M. Tinoco, S. Fernandez-Garcia, M. Lopez-Haro, A. B. Hungria, X. Chen, G. Blanco, J. A. Perez-Omil, S. E. Collins, H. Okuno and J. J. Calvino, *ACS Catal.*, 2015, **5**, 3504–3513.
33 F. Polo-Garzon, T. F. Blum, Z. Bao, K. Wang, V. Fung, Z. Huang, E. E. Bickel, D. Jiang, M. Chi and Z. Wu, *ACS Catal.*, 2021, **11**, 1938–1945.
34 M. Douthwaite, N. Powell, A. Taylor, G. Ford, J. M. López, B. Solsona, N. Yang, O. Sanahuja-Parejo, Q. He, D. J. Morgan, T. Garcia and S. H. Taylor, *ChemCatChem*, 2020, **12**, 3097–3107.
35 S. L. Bergman, J. Granestrand, Y. Tang, R. S. París, M. Nilsson, F. F. Tao, C. Tang, S. J. Pennycook, L. J. Pettersson and S. L. Bernasek, *Appl. Catal., B*, 2018, **220**, 506–511.
36 A. M. Motin, T. Haunold, A. V. Bukhtiyarov, A. Bera, C. Rameshan and G. Rupprechter, *Appl. Surf. Sci.*, 2018, **440**, 680–687.
37 F. J. Gracia, L. Bollmann, E. E. Wolf, J. T. Miller and A. J. Kropf, *J. Catal.*, 2003, **220**, 382–391.

38 N. Becknell, Y. Kang, C. Chen, J. Resasco, N. Kornienko, J. Guo, N. M. Markovic, G. A. Somorjai, V. R. Stamenkovic and P. Yang, *J. Am. Chem. Soc.*, 2015, **137**, 15817–15824.
39 M. J. Kale and P. Christopher, *ACS Catal.*, 2016, **6**, 5599–5609.
40 Z. Wang, C. Yang, T. Lin, H. Yin, P. Chen, D. Wan, F. Xu, F. Huang, J. Lin, X. Xie and M. Jiang, *Energy Environ. Sci.*, 2013, **6**, 3007–3014.
41 A. Lepcha, C. Maccato, A. Mettenbörger, T. Andreu, L. Mayrhofer, M. Walter, S. Olthof, T. P. Ruoko, A. Klein, M. Moseler, K. Meerholz, J. R. Morante, D. Barreca and S. Mathur, *J. Phys. Chem. C*, 2015, **119**, 18835–18842.
42 W. Zhou, W. Li, J. Q. Wang, Y. Qu, Y. Yang, Y. Xie, K. Zhang, L. Wang, H. Fu and D. Zhao, *J. Am. Chem. Soc.*, 2014, **136**, 9280–9283.
43 X. Chen, L. Liu, P. Y. Yu and S. S. Mao, *Science*, 2011, **331**, 746–750.
44 P. A. Carlsson, L. Österlund, P. Thormählen, A. Palmqvist, E. Fridell, J. Jansson and M. Skoglundh, *J. Catal.*, 2004, **226**, 422–434.
45 Z. An, H. Ma, H. Han, Z. Huang, Y. Jiang, W. Wang, Y. Zhu, H. Song, X. Shu, X. Xiang and J. He, *ACS Catal.*, 2020, **10**, 12437–12453.
46 H. J. Tong, J. Y. Yu, Y. H. Zhang and J. P. Reid, *J. Phys. Chem. A*, 2010, **114**, 6795–6802.
47 B. Köroğlu, Z. Loparo, J. Nath, R. E. Peale and S. S. Vasu, *J. Quant. Spectrosc. Radiat. Transfer*, 2015, **152**, 107–113.
48 J. Raskó, T. Kecskés and J. Kiss, *J. Catal.*, 2004, **224**, 261–268.
49 A. Vittadini, A. Selloni, F. P. Rotzinger and M. Grätzel, *J. Phys. Chem. B*, 2000, **104**, 1300–1306.
50 O. Gamba, H. Noei, J. Pavelec, R. Bliem, M. Schmid, U. Diebold, A. Stierle and G. S. Parkinson, *J. Phys. Chem. C*, 2015, **119**, 20459–20465.
51 C. E. Nanayakkara, J. K. Dillon and V. H. Grassian, *J. Phys. Chem. C*, 2014, **118**, 25487–25495.
52 S. T. Korhonen, M. Calatayud and A. Outi I Krause, *J. Phys. Chem. C*, 2008, **112**, 16096–16102.